This suggests the use of artificial nanostructures in CMR materials to achieve low-field MR in materials possessing intrinsic high-field MR. The present results on Cr-chalcogenides show that grain boundaries play less of a role than in the polycrystalline Mn-perovskite samples. This view is supported by the tendency of Cr-chalcogenides to form single crystals and the resultant high porosity of the present specimens. It would be of interest to increase the grain-boundary effect in the present system, either by varying the bulk synthesis route, or through thin-film techniques. ☐

Methods

The polycrystalline samples studied here were made by standard solid-state synthesis methods. Iron powder (99.9%), chromium powder (99.9%), sulphur powder (99.9995%) and copper powder (99.99%) were mixed in 2-g batches in the stoichiometric ratios and sealed into evacuated quartz tubes. The initial temperature was 450 °C, with slow increases in temperature in 50 °C increments up to 850 °C over a period of one week, with intermediate shakings and/or grinding until all signs of sulphur vapour and metal powder were eliminated. The resulting powder was then densified by pressing into pellets, (1/4 inch-diameter, 1/8 inch thick), re-sealed in a quartz tube and heated at 950 °C for three days. Phase purity was verified by X-ray powder diffraction of a small piece of the resultant pellet. Magnetization measurements were taken with a commercial magnetometer (Quantum Design Corp., San Diego, CA). Resistivity measurements were made using a four-probe in-line technique using an a.c. resistance bridge operating at 17 Hz. Thermopower data were taken using a commercial Seebeck-effect apparatus (MMR Corp., Mountain View, CA) referenced to a constantan standard.

1. Jonker, G. H. & Van Santen, J. H. Ferromagnetic compounds of manganese with perovskite structure. *Physica* **16**, 337–349 (1950).
2. Jin, S. *et al.* Thousandfold change in resistivity in magnetoresistive La-Ca-Mn-O films. *Science* **264**, 413–415 (1994).
3. Von Helmholt, R. *et al.* Giant negative magnetoresistance in perovskitelike La$_{2/3}$Ba$_{1/3}$MnO$_x$ Ferromagnetic films. *Phys. Rev. Lett.* **71**, 2331–2333 (1993).
4. Chahara, K. *et al.* Magnetoresistance in magnetic manganese oxide with intrinsic antiferromagnetic spin structure. *Appl. Phys. Lett.* **63**, 1990–1992 (1993).
5. Kusters, R. M. *et al.* Magnetoresistance measurements on the magnetic semiconductor Nd$_{0.5}$Pb$_{0.5}$MnO$_3$. *Physica B* **155**, 362–365 (1989).
6. Millis, A. J., Shraiman, B. I. & Mueller, R. Dynamic Jahn-Teller effect and colossal magnetoresistance in La$_{1-x}$Sr$_x$MnO$_3$. *Phys. Rev. Lett.* **77**, 175–178 (1996).
7. Röder, H., Zhang, J. & Bishop, A. R. *Phys. Rev. Lett.* **76**, 1356–1359 (1996).
8. Parkin, S. S. P. Giant magnetoresistance. *Annu. Rev. Mater. Sci.* **25**, 357–388 (1995).
9. Hwang, H. Y., Cheong, S.-W. & Batlogg, B. Enhancing the low-field magnetoresistive response in perovskite manganites. *Appl. Phys. Lett.* **68**, 3494–3496 (1996).
10. Sun, J. Z. *et al.* Observation of large low-field magnetoresistance in trilayer perpendicular transport devices made using doped manganite perovskites. *Appl. Phys. Lett.* **69**, 3266–3268 (1996).
11. Lu, Y. *et al.* Large magnetotunnelling effect at low magnetic fields in micrometer-scale epitaxial La$_{0.67}$Sr$_{0.33}$MnO$_3$ tunnel junctions. *Phys. Rev. B* **54**, 8357–8360 (1996).
12. Balzers, P. K., Wojtowicz, P. J., Robbins, M. & Lopatin, E. Exchange interactions in ferromatnetic chromium chalcogenide spinels. *Phys. Rev.* **151**, 367–377 (1966).
13. Goldstein, L. & Gibart, P. in *Proc. 17th Annu. Conf. on Magnetism and Magnetic Materials* (eds Graham, C.D. Jr. & Rhyne, J. J.) 883–886 (AIP Conf. Proc. No. 5 Am. Inst. Phys., New York, 1972).
14. Amith, A. & Gunsalus, G. L. Unique behavior of Seebeck coefficient in n-type CdCr$_2$Se$_4$. *J. Appl. Phys.* **40**, 1020–1022 (1969).
15. Haacke, G. & Beegle, L. C. Magnetic properties of the spinel system Fe$_{1-x}$Cu$_x$Cr$_2$S$_4$. *J. Phys. Chem. Solids* **28**, 1699–1704 (1967).
16. Haacke, G. & Beegle, L. C. Chalcogenide spinels. *J. Appl. Phys.* **39**, 656–657 (1968).
17. Haacke, G. & Beegle, L. C. Anomalous thermoelectric power of FeCr$_2$S$_4$ near the Curie temperature. *Phys. Rev. Lett.* **17**, 427–428 (1966).
18. Watanabe, T. Electrical properties of FeCr$_2$S$_4$ and CoCr$_2$S$_4$. *Solid State Commun.* **12**, 355–358 (1973).
19. Watanabe, T. & Nakada, I. Preparation of some chalcogenide spinel single crystals and their electronic properties. *Jpn. J. Appl. Phys.* **17**, 1745–1754 (1978).
20. Ando, K., Nishihara, Y., Okuda, T. & Tsushima, T. Hall effect and magnetoresistance in Fe$_{1-x}$Cu$_x$Cr$_2$S$_4$. *J. Appl. Phys.* **50**, 1917–1919 (1979).
21. Hwang, H. Y., Cheong, S.-W., Ong, N. P. & Batlogg, B. Spin-polarized intergrain tunneling in La$_{2/3}$Sr$_{1/3}$MnO$_3$. *Phys. Rev. Lett.* **77**, 2041–2044 (1996).
22. Urushibara, A. *et al.* Insulator-metal transition and giant magnetoresistance in La$_{1-x}$Sr$_x$MnO$_3$. *Phys. Rev. B* **51**, 14103–14109 (1995).
23. Lotgering, F. K., Van Stapele, R. P., Van Der Steen, G. H. A. M. & Wieringen, J. S. Magnetic properties of conductivity and ionic ordering in Fe$_{1-x}$Cu$_x$Cr$_2$S$_4$. *J. Phys. Chem. Solids* **30**, 799–804 (1969).
24. Kogan, E. M. & Auslender, M. I. Anderson localization in ferromagnetic semiconductors due to spin disorder. *Phys. Stat. Sol. B* **147**, 613–620 (1988).
25. Shimakawa, Y., Kubo, Y. & Manako, T. Giant magnetoresistance in Tl$_2$Mn$_2$O$_7$ with the pyrochlore structure. *Nature* **379**, 53–55 (1996).
26. Cheong, S.-W., Hwang, H. Y., Batlogg, B. & Rupp, L. W. Jr. Giant magnetoresistance in pyrochlore Tl$_{2-x}$In$_x$Mn$_2$O$_7$. *Solid State Commun.* **98**, 163–166 (1996).
27. Subramanian, M. A. *et al.* Colossal magnetoresistance without Mn^{3+}/Mn^{4+} double exchange in stoichiometric pyrochlore Tl$_2$Mn$_2$O$_7$. *Science* **273**, 81–84 (1996).

Clocking transient chemical changes by ultrafast electron diffraction

J. Charles Williamson, Jianming Cao, Hyotcherl Ihee, Hans Frey & Ahmed H. Zewail

Arthur Amos Noyes Laboratory of Chemical Physics, California Institute of Technology, Pasadena, California 91125, USA

With the advent of femtosecond (fs) time resolution in spectroscopic experiments, it is now possible to study the evolution of nuclear motions in chemical and photobiochemical reactions. In general, the reaction is clocked by an initial fs laser pulse (which establishes a zero of time) and the dynamics are probed by a second fs pulse; the detection methods include conventional and photoelectron spectroscopy and mass spectrometry[1-4]. Replacing the probe laser with electron pulses offers a means for imaging ultrafast structural changes with diffraction techniques[5-8], which should permit the study of molecular systems of greater complexity (such as biomolecules). On such timescales, observation of chemical changes using electron scattering is non-trivial, because space-charge effects broaden the electron pulse width and because temporal overlap of the (clocking) photon pulse and the (probe) electron pulse must be established. Here we report the detection of transient chemical change during molecular dissociation using ultrafast electron diffraction. We are able to detect a change in the scattered electron beam with the zero of time established unambiguously and the timing of the changes clocked *in situ*. This ability to clock changes in scattering is essential to studies of the dynamics of molecular structures.

Diffraction methods, generally utilizing X-rays or electrons, are direct approaches for determining complex structures at microscopic dimensions[9-14]. Techniques for creating ultrashort, coherent and collimated X-ray pulses are still in their infancy, and at present the X-ray flux from most sources is relatively low. For gas-phase ultrafast electron diffraction (UED) to succeed, major challenges must be surmounted. First, because the number densities of gas samples are orders of magnitude lower than solids and surfaces, gas-phase diffraction intensities are very weak. Second, there is no long-range order to enhance coherent interferences, and thus the incoherent background scattering from gases is orders of magnitude greater. Last, there has not previously been a way to determine *in situ* the zero of time in UED experiments.

In gas-phase electron diffraction (GED) the scattering intensity decreases as the fourth power of the momentum transfer $s = (4\pi/\lambda)\sin(\theta/2)$, where λ is the de Broglie wavelength of the electrons and θ is the scattering angle. Conventional GED experiments require a high electron flux (of the order of microamperes) to yield internuclear separations with precision on the order of 0.001 Å (ref. 15). Over the past two decades, the speed of GED experiments has improved to the micro- and nanosecond timescale. Microsecond studies include time-of-flight investigations of molecular clusters[16], and photodissociation experiments where the electron beam is electromagnetically chopped[17,18]. A temporal resolution of 15 ns has been achieved with a pulsed laser driven electron source[19].

In order to probe ps and sub-ps changes and the associated orientational anisotropy[20] with UED, three basic experiments must be incorporated into our apparatus: measurement of the electron pulsewidth, accurate clocking of the reaction, and detection of single electrons (necessary to reduce the electron flux and minimize space-charge broadening). To this end we have developed the new apparatus shown in Fig. 1, representative of a second generation of

diffraction experiments in our laboratories[6,8]. The apparatus is composed of a fs laser, an ultrafast electron gun, a free-jet expansion source, and a newly designed two-dimensional single-electron detection system. Femtosecond laser pulses were created from a colliding-pulse mode-locked ring dye laser. The output from this laser was directed through a four-stage pulsed dye amplifier with no pulse compression (620 nm, 2–3 mJ, 30 Hz, 300 fs). For initiation of the reaction, 95% of this beam was doubled (310 nm, ~250 μJ). The remainder (also doubled) was focused onto a back-illuminated, negatively-biased photocathode to generate the electron pulse via the photoelectric effect.

The ejected photoelectrons were accelerated into a series of electrostatic lenses that collimate and focus the electron beam; for 19 keV, λ is 0.088 Å. The position of the electron beam was controlled with horizontal and vertical deflectors. Two closely spaced metal plates were used for streaking experiments. The vacuum system was divided into two chambers and differentially pumped (Fig. 1). The sample molecules entered the vacuum chamber in a free-jet expansion mounted on an xyz positioning stage. The scattering chamber background pressure with gas flow was ~2 × 10^{-4} torr. Both chambers were shielded with μ-metal to reduce the effects of the Earth's magnetic field.

The component most critical to the success of UED is the detection system. The electron flux must be very low in order to keep the temporal resolution ultrafast. Early on we recognized that all of the scattered electrons must be detected for the experiment to succeed[6], and we introduced the two-dimensional charge-coupled

device (CCD) as a detector in a direct electron bombardment mode[8]. To increase the longevity and flexibility of the single-electron detection system, our second-generation apparatus now employs two CCDs: one is a small, direct-bombardment device installed in the scattering chamber, and the other is a large, scientific-grade device mounted in a separate chamber at the end of a phosphor scintillator/fibre optic/image intensifier chain. Details will be published elsewhere.

To confirm the time resolution of the apparatus, we have measured the electron pulse duration *in situ* as a function of the number of electrons per pulse using the high-speed deflection technique in a streak camera arrangement. Streak velocities (which measure the conversion from temporal to spatial resolution, as shown in Fig. 2) attained with this setup are on the order of 1.6 × 10^8 m s^{-1}, or ~2 pixels per ps on the detector. The resolution of the streak experiment is therefore ±0.5 ps. Steak images spanning three orders of magnitude of electron number are shown in Fig. 2.
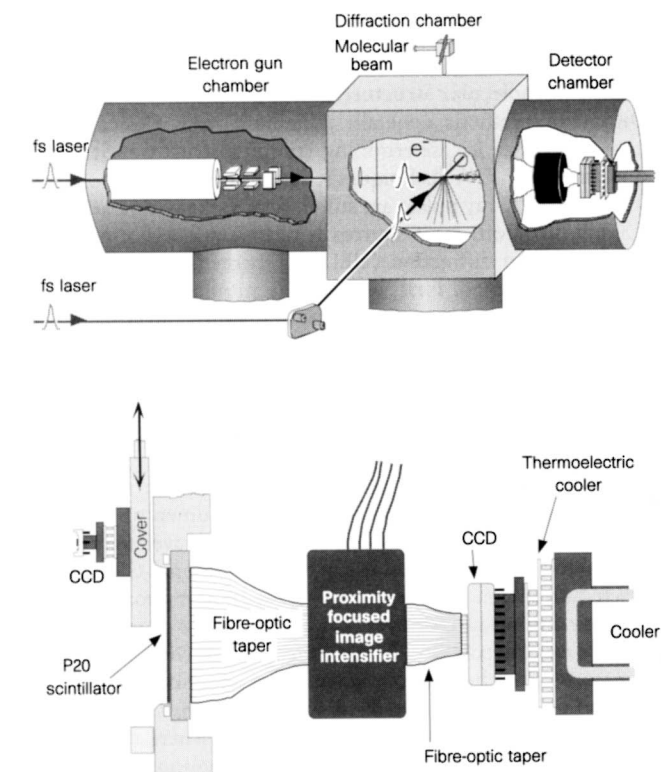

Figure 1 Top, second-generation ultrafast electron diffraction apparatus, consisting of an electron gun chamber, a diffraction chamber and a detector chamber. Two fs laser pulses are used; the first initiates the chemical change and the second generates the electron pulse. Bottom, detection scheme. Incident electrons either directly bombard a small CCD or strike a phosphor-coated fused fibre-optic window. Light emitted from the phosphor is amplified by an image intensifier and brought to a scientific-grade CCD. Both CCDs are thermoelectrically cooled.
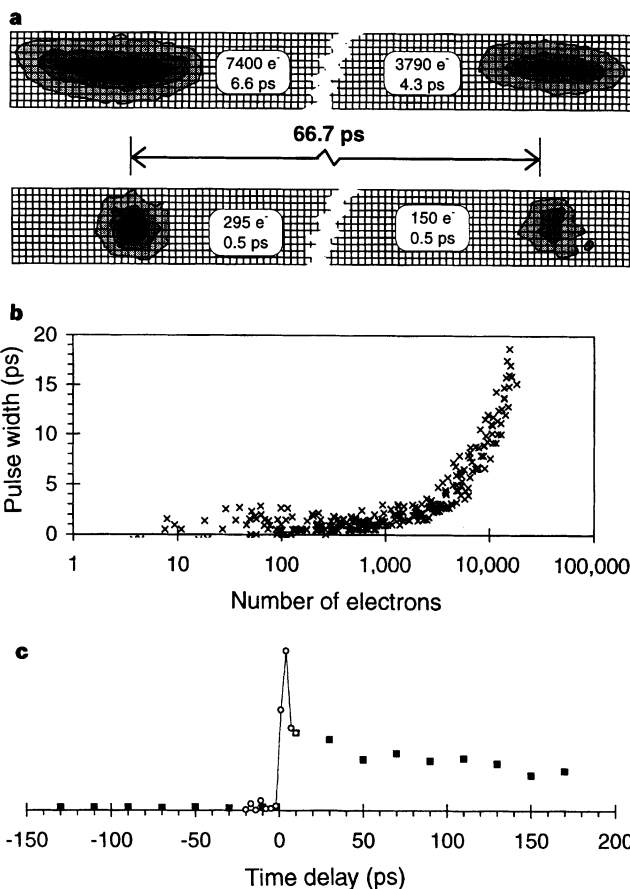

Figure 2 a, Surface contour plots of low- and high-intensity streaked electron pulse pairs. Each pair comes from two incident light pulses, one of which is delayed by 66.7 ps. The horizontal coordinate is the steaking axis. The temporal durations of pulses with high electron numbers (top trace: 7,400 e$^-$, 6.6 ps; 3,790 e$^-$, 4.3 ps) are broadened by space-charge effects. For low electron numbers (bottom trace: 295 e$^-$, 0.5 ps; 150 e$^-$, 0.5 ps), measurement of the pulse width is limited by the resolution of the streak experiment. The electron pulse width was obtained by subtracting the width of the unstreaked electron beam (4 pixels) from the width of the streaked pulses (lorentzian profiles). **b**, Measured electron pulse widths as a function of the number of electrons. The streak velocity was 2.1 pixels per ps, or 1.6 × 10^8 m s^{-1}. The sweep voltage is ~1 kV ns^{-1}. **c**, Experimental photoionization-induced lensing transient. The ordinate reflects the relative difference between the average profile of the electron beam spot in the presence of the excitation laser and a reference profile (no laser).

For electron intensities on the order of 10^4 electrons per pulse, the width is typically ~10 ps. The laser and electron beam waists at overlap was measured to be $450 \pm 50\ \mu m$, so the velocity mismatch contribution[7] to the total experimental temporal resolution is ~4 ps.

To clock chemical changes, we must establish the zero of time (t_0). A streak camera[9] or photo-triggered deflection plates[21] can give t_0 to within 10–20 ps, but these methods require some extrapolation and do not duplicate the design of crossed-beam experiments. Another approach is to rely on changes in the diffraction pattern of the system under investigation, but this is not an independent means of finding t_0. More importantly, this method is simply not practical for gas-phase work because of the long integration times required to obtain a single data point.

In the clocking technique developed here for UED, we use the crossed-beam geometry of the actual diffraction experiment, rather than relying on scattered electrons. The idea is to let the initiation laser pulse create a coulombic field (by ionization), which deflects the unscattered electron beam only during and after the laser pulse passes through. The phenomenon, termed lensing, occurs because the field focuses the charged electron beam. Fig. 2 shows the degree of lensing versus time; the lensing is a maximum when the laser and electron pulses are temporally overlapped. The results accurately show the precise $t = 0$ (to ~2 ps) and hence allow a direct clocking of changes in the diffraction experiment with ps resolution. We recorded lensing transients as a function of the position, polarization and diameter of the pump laser, and conducted control experiments where no gas was flowing and where the sample source tip was far removed from or close to the interaction region.

After successfully establishing t_0, we conducted the first time-resolved gas-phase electron diffraction experiment with picosecond resolution. Diiodomethane (CH_2I_2) was selected as our prototype system because the loss of an iodine atom after dissociation at 310 nm is a major structural change which occurs in less time than the rotational period (~10 ps)[22,23]. To clock the change, diffraction images were recorded on the CCD at delays of -20 ps, 0 ps, and up to $+70$ ps (Figs 3 and 4).

The experimental modified molecular scattering intensity, $sM(s)$, was obtained at each time point

$$sM(s) = s\,\frac{I_{\mathrm{tot}}(s) - I_{\mathrm{back}}(s)}{|f_a|\,|f_b|} \qquad (1)$$

where I_{tot} is the total scattering intensity, I_{back} is the background (including atomic) scattering intensity, and f_a and f_b are atomic scattering amplitudes[15,19]. Typical $sM(s)$ raw data taken at -20 ps

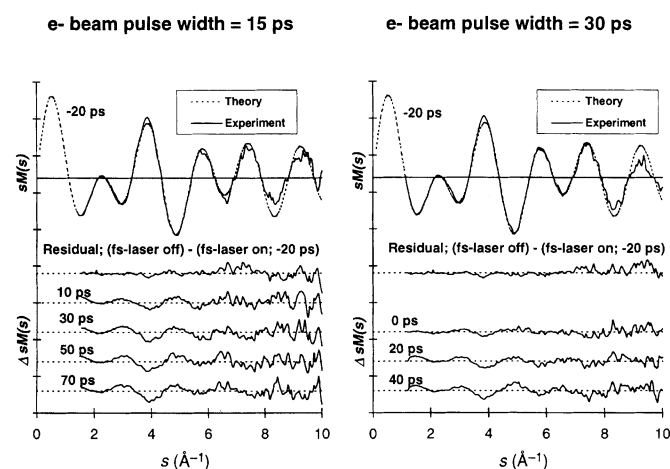**e- beam pulse width = 15 ps**   **e- beam pulse width = 30 ps**

Figure 3 Experimental modified molecular scattering curves for two sets of data taken with 15-ps (left panel) and 30-ps (right panel) electron pulses. The delay times between the fs laser pulse and the ps electron pulse are shown. Theoretical calculations of $sM(s)$ at -20 ps are presented (see text).

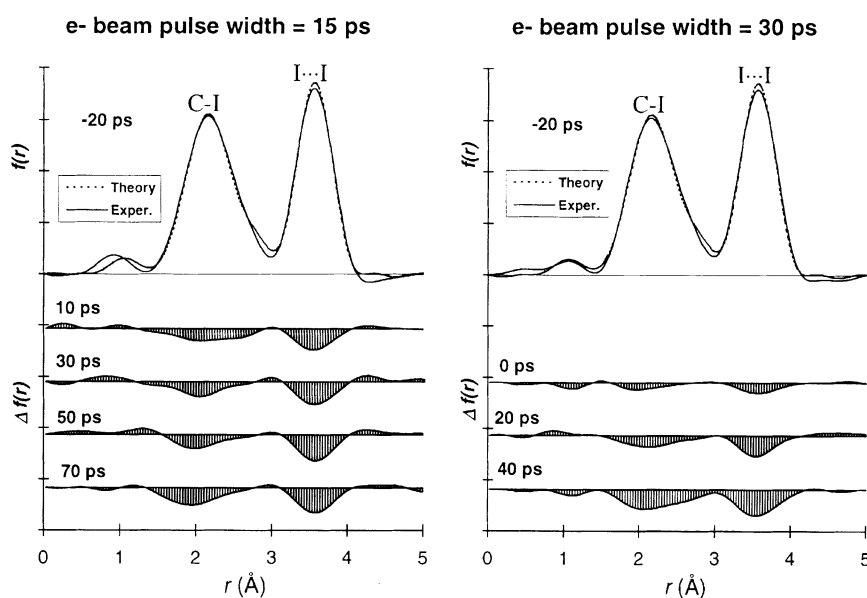**e- beam pulse width = 15 ps**   **e- beam pulse width = 30 ps**

Figure 4 Radial distribution functions $f(r)$ and $\Delta f(r)$ obtained from the $sM(s)$ and $\Delta sM(s)$ curves of Fig. 3, also for two sets of data (15-ps and 30-ps electron pulse width, left and right panel, respectively). The corresponding theoretical $f(r)$ curve for the -20 ps data is shown. The changes obtained are in the region of the C–I and I···I internuclear separations (see text). Note that in $f(r)$ the peak corresponding to the I···I distance should have about twice the area of the first peak (C–I and H···I); the peak area scales approximately as $n_{ij}Z_iZ_j/r_{ij}$ (where Z is the atomic number and n is the multiplicity for nuclear pairs). However, because of damping in equation (2), the peaks appear to be of equal areas, and this is evident in our simulations for different values of k. The theoretical simulations shown in the figure are based on the structural data of ref. 24. We have also used more recent data from K. Hedberg's and co-workers (personal communication) and obtained very similar $f(r)$ curves (data not shown), within the reported resolution.

are shown in Fig. 3. The theoretical fits, calculated from structural parameters[24] (see also Fig. 4 legend) of CH_2I_2, are superimposed on the experimental data. To unambiguously establish the magnitude of the change with time, we also recorded the $sM(s)$ in the absence of the fs initiation laser and obtained the residual of that $sM(s)$ minus the $sM(s)$ taken at -20 ps. This residual is essentially flat (Fig. 3), indicating that the two are identical. Thus, the $sM(s)$ at -20 ps is a calibration point in time, independent of any theoretical fit. The change in the diffraction pattern as a function of time is shown in two sets of data having differing temporal resolutions (15 ps and 30 ps); the $\Delta sM(s)$ curves are relative to the -20 ps data.

Radial distribution curves were obtained from the $sM(s)$ curves according to the standard GED equation:

$$f(r) = \int_0^{s_{max}} sM(s)\sin(sr)\exp(-ks^2)ds \qquad (2)$$

where the constant k is a damping coefficient included for the limited s range. Figure 4 shows the experimental and theoretical $f(r)$ obtained from the -20 ps $sM(s)$ curves of Fig. 3. The time-evolution of $\Delta f(r)$ is also presented for the two sets of data. At positive time the amplitudes of the dominating C–I and I$\cdots$I peaks decrease, corresponding to the loss of an iodine atom. Both the $sM(s)$ and $f(r)$ representations of our diffraction data clearly show a chemical change occurring as the delay between the fs laser pulse and the ps electron pulse sweeps from negative, to zero, and to positive times. From the $f(r)$ data, we obtained the standard deviation for more than 100 diffraction images for each data set, and established that the signal-to-noise ratio is better than 60. Thus, we could detect a change as small as 3%, which is a factor of 5 less than the changes reported here.

Breakage of one C–I bond reduces the I$\cdots$I peak twice as quickly as the C–I peak because CH_2I_2 has two C–I bonds and one I$\cdots$I internuclear separation. This is observed in our data, corroborated by theoretical simulations of $f(r)$ (not shown) which account for the percentage change of CH_2I_2 to CH_2I and I. Similar time-resolved studies were made for $C_2F_4I_2$ and CHI_3. Quantitative analysis in the future should yield the changes due to the second C–I bond breakage, and elucidate the structure of the intermediate. Last, ground-state diffraction patterns of three other molecules (CF_3I, CCl_4 and SF_6) were recorded with our new UED apparatus (data not shown). As mentioned earlier, the diffraction patterns were converted to experimental $sM(s)$ curves and radial distribution functions. The experimental and theoretical agreement is very good.

From the results presented here, it is now evident that ultrafast electron diffraction has achieved the temporal resolution and detection sensitivity necessary for picosecond and subpicosecond studies of complex molecular systems. In future work, utilizing modulation and difference detection techniques, efforts will be directed toward the suppression of background scattering from unreactive species so that molecular structural changes can be analysed with precision. ☐

1. Chergui, M. (ed.) *Femtochemistry: Ultrafast Chemical and Physical Processes in Molecular Systems* (World Scientific, Singapore, 1996).
2. Manz, J. & Wöste, L. (eds) *Femtosecond Chemistry* (VCH, New York, 1995).
3. Zewail, A. H. *Femtochemistry: Ultrafast Dynamics of the Chemical Bond* (World Scientific, Singapore, 1994).
4. Manz, J. & Castleman, A. W. Femtochemistry. *J. Phys. Chem.* (spec. iss.) **97**(48), 12423–12649 (1993).
5. Williamson, J. C. & Zewail, A. H. Structural femtochemistry: experimental methodology. *Proc. Natl Acad. Sci. USA* **88**, 5021–5025 (1991).
6. Williamson, J. C., Dantus, M., Kim, S. B. & Zewail, A. H. Ultrafast diffraction and molecular structure. *Chem. Phys. Lett.* **196**, 529–534 (1992).
7. Williamson, J. C. & Zewail, A. H. Ultrafast electron diffraction. Velocity mismatch and temporal resolution in crossed-beam experiments. *Chem. Phys. Lett.* **209**, 10–16 (1993).
8. Dantus, M., Kim, S. B., Williamson, J. C. & Zewail, A. H. Ultrafast electron diffraction. 5. Experimental time resolution and applications. *J. Phys. Chem.* **98**, 2782–2796 (1994).
9. Ràksi, F. *et al.* Ultrafast x-ray absorption probing of a chemical reaction. *J. Chem. Phys.* **104**, 6066–6069 (1996).
10. Tomov, I. V., Chen, P. & Rentzepis, P. M. Picosecond time-resolved x-ray diffraction during laser-pulse heating of an Au(111) crystal. *J. Appl. Crystallogr.* **28**, 358–362 (1995).
11. Kim, K.-J., Chattopadhyay, S. & Shank, C. V. Generation of femtosecond X-rays by 90-degrees Thomson scattering. *Nucl. Instr. Meth. Phys. Res. A* **341**, 351–354 (1994).
12. Williamson, S., Mourou, G. & Li, J. C. M. Time-resolved laser-induced phase transformation in aluminum. *Phys. Rev. Lett.* **52**, 2364–2367 (1984).
13. Elsayed-Ali, H. E. Time-resolved reflection high-energy electron diffraction of metal surfaces. *Proc. SPIE* **2521**, 92–102 (1995).
14. Aeschlimann, M. *et al.* A picosecond electron gun for surface analysis. *Rev. Sci. Instrum.* **66**, 1000–1009 (1995).
15. Hargittai, I. & Hargittai, M. (eds) *Stereochemical Applications Of Gas-Phase Electron Diffraction* (VCH, New York, 1988).
16. Dibble, T. S. & Bartell, L. S. Electron diffraction studies of the kinetics of phase changes in molecular clusters. 3. Solid-state phase transformations in SeF_6 and $(CH_3)_3CCl$. *J. Phys. Chem.* **96**, 8603–8610 (1992).
17. Ischenko, A. A. *et al.* A stroboscopical gas-electron diffraction method for the investigation of short-lived molecular species. *Appl. Phys. B* **32**, 161–163 (1983).
18. Rood, A. P. & Milledge, J. Combined flash-photolysis and gas-phase electron diffraction studies of small molecules. *J. Chem. Soc. Faraday Trans. 2* **80**, 1145–1153 (1984).
19. Ischenko, A. A., Schäfer, L., Luo, J. Y. & Ewbank, J. D. Structural and vibrational kinetics by stroboscopic gas electron diffraction: the 193 nm photodissociation of CS_2. *J. Phys. Chem.* **98**, 8673–8678 (1994).
20. Williamson, J. C. & Zewail, A. H. Ultrafast electron diffraction. 4. Molecular structures and coherent dynamics. *J. Phys. Chem.* **98**, 2766–2781 (1994).
21. Williamson, S., Mourou, G. & Letzring, S. Picosecond electron diffraction. *Proc. SPIE* **348**, 313–317 (1983).
22. Kawasaki, M., Lee, S. J. & Bersohn, R. Photodissociation of molecular beams of methylene iodide and iodoform. *J. Chem. Phys.* **63**, 809–814 (1975).
23. Baughcum, S. L. & Leone, S. R. Photofragmentation infrared emission studies of vibrationally excited free radicals CH_3 and CH_2I_2. *J. Chem. Phys.* **72**, 6531–6545 (1980).
24. Hassel, O. & Viervoll, H. Electron diffraction investigation of molecular structure II, results obtained by the rotating sector method. *Acta Chem. Scand.* **1**, 149–168 (1947).

Three-dimensional self-assembly of millimetre-scale components

Andreas Terfort, Ned Bowden & George M. Whitesides

Department of Chemistry and Chemical Biology, Harvard University, 12 Oxford Street, Cambridge, Massachusetts 02138, USA

The spontaneous association of molecules, termed molecular self-assembly, is a successful strategy for the generation of large, structured molecular aggregates[1]. The most important source of inspiration for this strategy is the biological world, in which many processes involve interfacial interactions and shape selectivity that guide the formation of complex, multicomponent three-dimensional structures. The success of molecular self-assembly notwithstanding, many objectives in science and technology require the assembly of components that are much larger than molecules: examples include microelectronic and microelectro-mechanical systems, sensors and microanalytical and micro-synthetic devices[2]. Photolithography, the principal technique used to make such microstructures, has certain limitations: it cannot easily form non-planar or three-dimensional structures; it generates structures that are metastable; and it can be used only for a limited set of materials[3]. Here we describe an approach for the self-assembly of millimetre-scale components that uses two concepts to direct the assembly process: shape recognition and the minimization of liquid–liquid interfacial free energies[4]. These play a role in other spontaneous self-assembly phenomena, such as the formation of bubble rafts[5,6], the patterned dewetting of surfaces[7,8], and the coalescence of liquid drops[9]. We apply self-assembled monolayer molecular films[10] to the surfaces of shaped macroscopic objects to render them hydrophilic or hydrophobic, depending on the terminal groups of the bound molecules. In aqueous solution, hydrophobic surfaces bearing a thin film of a